

UC Berkeley

UC Berkeley Previously Published Works

Title

Enhanced surface urban heat islands due to divergent urban-rural greening trends

Permalink

<https://escholarship.org/uc/item/7z3453c6>

Journal

Environmental Research Letters, 16(12)

ISSN

1748-9318

Authors

Chen, Chi

Li, Dan

Keenan, Trevor F

Publication Date

2021-12-01

DOI

10.1088/1748-9326/ac36f8

Copyright Information

This work is made available under the terms of a Creative Commons Attribution License, available at <https://creativecommons.org/licenses/by/4.0/>

Peer reviewed

LETTER • OPEN ACCESS

Enhanced surface urban heat islands due to divergent urban-rural greening trends

To cite this article: Chi Chen *et al* 2021 *Environ. Res. Lett.* **16** 124071

View the [article online](#) for updates and enhancements.

You may also like

- [Reduction in human activity can enhance the urban heat island: insights from the COVID-19 lockdown](#)
TC Chakraborty, Chandan Sarangi and Xuhui Lee
- [A high density urban temperature network deployed in several cities of Eurasian Arctic](#)
Pavel Konstantinov, Mikhail Varentsov and Igor Esau
- [Decline in surface urban heat island intensity in India during heatwaves](#)
Rahul Kumar and Vimal Mishra

ENVIRONMENTAL RESEARCH
LETTERS

LETTER

Enhanced surface urban heat islands due to divergent urban-rural greening trends

OPEN ACCESS

RECEIVED
6 October 2021REVISED
1 November 2021ACCEPTED FOR PUBLICATION
5 November 2021PUBLISHED
16 December 2021

Original content from this work may be used under the terms of the [Creative Commons Attribution 4.0 licence](#).

Any further distribution of this work must maintain attribution to the author(s) and the title of the work, journal citation and DOI.

Chi Chen^{1,2,*} , Dan Li³  and Trevor F Keenan^{1,2} ¹ Department of Earth and Environmental Sciences, Lawrence Berkeley National Laboratory, Berkeley, CA 94720, United States of America² Department of Environmental Science, Policy and Management, UC Berkeley, Berkeley, CA 94720, United States of America³ Department of Earth and Environment, Boston University, Boston, MA 02215, United States of America

* Author to whom any correspondence should be addressed.

E-mail: chenchi@lbl.gov**Keywords:** Earth greening, leaf area index, land surface temperature, urban heat island, land surface energy budget, trendSupplementary material for this article is available [online](#)**Abstract**

Satellite observations show that the surface urban heat island intensity (SUHII) has been increasing over the last two decades. This is often accompanied by an increased urban-rural contrast of vegetation greenness. However, the contribution of uneven vegetation trends in urban and rural areas to the trend of SUHII is unclear, due to the confounding effects of climate change and changes in man-made infrastructures and anthropogenic heat sources. Here we use a data-model fusion approach to quantify such contributions during the peak growing season. We show that the LAI_{dif} (the urban-rural difference of leaf area index) is increasing ($P < 0.05$) in 189 of the selected 228 global megacities. The increasing trend of LAI_{dif} from 2000 to 2019 accounts for about one quarter of the trend in satellite-derived SUHII, and the impact is particularly evident in places with rapid urbanization and rural cropland intensification. The marginal sensitivity of SUHII to LAI_{dif} is the strongest in hot-humid megacities surrounded by croplands and in hot-dry megacities surrounded by mixed woody and herbaceous vegetation. Our study highlights the role of long-term vegetation trends in modulating the trends of urban-rural temperature differences.

1. Introduction

Today more than 55% of the world's population lives in urban areas and this number will reach 68% by 2050 (United Nations 2019). Urbanization is one of the most visible anthropogenic land use/land cover changes (Weng *et al* 2004, Peng *et al* 2012). In addition to producing anthropogenic heat fluxes, urbanization alters many other aspects of the surface energy budget, resulting in higher surface and near-surface temperatures in cities than their rural surroundings, a phenomenon known as the urban heat island (UHI) effect (Zhao *et al* 2014, Oke *et al* 2017, Manoli *et al* 2019, Li *et al* 2019a). With global warming (Hansen *et al* 2010), the combined effects of UHIs and heatwaves will pose significant threats to public health (Kovats and Hajat 2008, Li and Bou-Zeid 2013, Mora *et al* 2017, Liao *et al* 2018a, 2021) and increase the

global cooling power consumption (Li *et al* 2019b). Previous studies suggest that the spatial variations of the surface UHI intensity (SUHII), which is defined as the difference of land surface temperature (LST) between urban and rural areas, are strongly controlled by background climates and mainly follow the precipitation gradient, but the spatial variations of SUHII with biome types remain elusive (Kalnay and Cai 2003, Zhao *et al* 2014, Zhou *et al* 2016, Manoli *et al* 2019, Li *et al* 2019a).

Vegetation is a key control of land-atmosphere interactions. Changes in vegetation characteristics affect the surface energy budget through altering radiation, convection, evapotranspiration (ET), and heat storage (Sellers *et al* 1997, Peng *et al* 2012, Li *et al* 2014, Zhao *et al* 2014, Chen *et al* 2020a, Wang *et al* 2020a). Contrast in vegetation greenness between urban and rural areas is found to be

significantly correlated with the SUHII (Weng *et al* 2004, Oleson 2012, Peng *et al* 2012, Chakraborty and Lee 2019). Owing to land-use management and climate change, trends in vegetation greenness over urban and rural areas are often different, which can either enhance or reduce the urban-rural vegetation contrast, thereby altering the SUHII (Oleson 2012, Li *et al* 2016). Satellite observations show widespread enhancements in leaf area index (LAI) surrounding built-up areas (Chen *et al* 2019). Meanwhile, many urban areas become comparably less green, or exhibit declines in vegetation greenness, and are expected to become more impervious (Seto *et al* 2012, Schneider *et al* 2015). Yao *et al* suggest that the global rural greening trend correlates with the increasing trend of satellite-derived SUHII (2019). However, it is unclear the extent to which the SUHII trend is directly caused by the biophysical effects of uneven vegetation changes between urban and rural areas (Chakraborty and Lee 2019), which is confounded by the simultaneous changes in climatic conditions, anthropogenic heat fluxes, and man-made infrastructures (Kalnay and Cai 2003, Zhao *et al* 2014, Li *et al* 2019a).

Here we aim to quantify the contribution of vegetation's long-term trend to the SUHII trend (trends are henceforth indicated by Δ). We study LST instead of near-surface air temperatures because LST is directly constrained by the surface energy balance equation (Chen *et al* 2020a) and its apparent change is observable from satellites. It has been reported that the SUHII is several folds stronger than the intensity of near-surface air UHI, making it easier to detect the vegetation biophysical effects (Venter *et al* 2021). We use a process-based attribution framework (the two-resistance mechanism method, TRM) to isolate the effect of LAI_{dif} trend on the SUHII trend (Rigden and Li 2017, Liao *et al* 2018b, 2021, Li and Wang 2019, Wang *et al* 2019, 2020b, Li *et al* 2019a, Moon *et al* 2020, Chen *et al* 2020a, 2020b, Wang and Li 2021) (see section 2 and supplementary information (available online at stacks.iop.org/ERL/16/124071/mmedia)). This framework is based on the surface energy balance equation in which changes in vegetation greenness primarily alter the albedo for shortwave radiation, the aerodynamic resistance for scalar transfers, the surface resistance for water vapor transfer, the ground heat flux, and the emissivity (Chen *et al* 2020a). Acknowledging that the mechanism causing SUHII differ between daytime and nighttime (Peng *et al* 2012, Yang *et al* 2021) as a starting point we analyze the impacts of vegetation dynamics on the trends of daily average SUHII. We focus on the peak growing seasons, the three consecutive months with the largest mean LAI, during which the vegetation biophysical effects on LST are the strongest (Imhoff *et al* 2010, Peng *et al* 2012).

2. Methods

2.1. Land cover and definition of urban and rural patches

Land cover information is provided by the Collection 6 Moderate Resolution Imaging Spectroradiometer (MODIS) land cover product (MCD12C1, yearly, $0.05^\circ \times 0.05^\circ$) (Friedl and Sulla-Menashe 2015). We use the International Geosphere-Biosphere Programme (IGBP) classification layer to define contiguous urban and rural areas (figure S1). First, a pixel is termed urban if it is classified as 'urban and built-up lands' by IGBP in any year between 2001 to 2018. This allows us to capture a maximum possible urban extent in the presence of urbanization, and is equivalent to assuming that a pixel can be transformed into an urban area and that the process is irreversible (Schneider 2012). A fixed urban extent also makes the trend of urban LAI unambiguous since allowing the urban extent to vary might cause an LAI trend even if the LAI of each pixel does not change. This implemented, a fixed urban extent effectively captures the underlying vegetation changes due to urban footprint changes (Yang *et al* 2019). Second, we label all adjacent urban pixels (i.e. eight-neighbours) as an urban patch. Each urban patch must have at least 16 pixels, which is about 493 km^2 at the equator. Third, in order to match the resolution of the reanalysis data (i.e. the enhanced land component of the European Centre for Medium-Range Weather Forecasts Reanalysis, or ERA5-Land), we aggregate the pixels within each urban patch from $0.05^\circ \times 0.05^\circ$ to $0.1^\circ \times 0.1^\circ$ resolution. During the aggregation process, a coarse-resolution pixel is marked as urban only if at least two of the four fine-resolution pixels are classified as urban (Schneider *et al* 2009). We repeat the second step to further merge the adjacent urban patches newly produced by the aggregation. Fourth, after identifying the urban patch, we define the rural patch as a surrounding 0.1° -buffer zone ($\sim 11 \text{ km}$), which allows the urban and rural areas to be approximately equal. Rural patches include only land pixels. Finally, we term a pair of urban and rural patches as a megacity. We analyze 228 megacities worldwide after excluding five megacities where the TRM framework fails due to negative aerodynamic or surface resistances (physically meaningless) (Liao *et al* 2018b). They are Cape Town (South Africa), Samarkand (Uzbekistan), Lahore (Pakistan), Almaty (Kazakhstan), and Dalian (China). Due to the spatial aggregation in our pre-processing of the land cover data, some megacities consist of multiple geometrically contiguous municipal cities, such as megacities of the Rhine-Ruhr (Germany), New York and Philadelphia (USA), the Greater Los Angeles (USA), the Pearl River Delta (China), the Yangtze River Delta (China), and the Tokyo Capital Region (Japan), etc. We note that the uncertainties in the MODIS land

cover maps may propagate to the identification of urban and rural areas (Friedl *et al* 2002). Since our study focuses more on LST and LAI contrasts between urban and rural areas and their associated changes at the patch scale the accuracy of urban patch identification should be sufficient for this study.

2.2. MODIS LAI and LST

MODIS Collection 6 LAI products (MOD15A2H and MYD15A2H) are used in this study (Myneni *et al* 2015a, 2015b), which are 500 m, eight day composites. Ground data have been used to verify the quality of the LAI products (Yan *et al* 2016a, 2016b), and these products have been widely used in previous work (Chen *et al* 2019, Piao *et al* 2020). In this study, the LAI products are filtered with quality flags and composited to monthly averages using the number of days as the weight of each original eight day composite. We exclude pixels contaminated by clouds, aerosols, shadows, snow, and ice, and fill the gaps using the climatological mean monthly LAI during the study period (Samanta *et al* 2011, Chen *et al* 2019). The monthly LAI is further aggregated to $0.1^\circ \times 0.1^\circ$ and averaged to obtain the peak growing season mean. The peak growing season is defined as the three consecutive months with the highest mean LAI for each three month moving window (figure S2(a)). Then we calculate the average LAI for urban and rural patches (figure S3), as well as their difference (LAI_{dif}), for each megacity. Finally, LAI trends (ΔLAI) are estimated using the Mann-Kendall test.

The MODIS LST products (i.e. MOD11C3 and MYD11C3) are used to compute SUHII for each megacity ($0.05^\circ \times 0.05^\circ$, monthly composite, 2000–2019) (Wan *et al* 2015a, 2015b). We average the daytime and the nighttime LSTs, and use the average as a proxy for daily mean LST. According to the product user guide, the following quality filtering is applied: ‘Mandatory QA flags’, ‘Emissivity Error flag’ and ‘LST Error flag’ have to be ‘00’ or ‘01’; ‘Data quality flag’ has to be ‘0’. All MODIS LST data are converted to the same spatial and temporal resolution as the LAI data. We note that the MODIS SUHII is not used to calculate the impact of vegetation trend on the SUHII trend, which is diagnosed by the attribution method in section 2.5. The trend in MODIS SUHII is a result of vegetation biophysical effects, human-induced effects, and large-scale atmospheric changes (Zhou *et al* 2019).

2.3. ERA5 reanalysis

We use monthly averaged variables from ERA5-Land reanalysis ($0.1^\circ \times 0.1^\circ$, diel average, 2000–2019) as inputs for the attribution framework described in section 2.5, including albedo (α), surface solar radiation downwards (S_{in}), surface thermal radiation downloads (L_{in}), surface net thermal radiation (L_{net}),

surface latent heat flux (LE), surface sensible heat flux (H), and surface pressure (P_s) (Muñoz-Sabater 2019). Further, aridity index is calculated as the ratio of annual precipitation (Pr) to potential evapotranspiration (PET). ERA5-Land is a replay of the land component of the ERA5 reanalysis with an improved spatial resolution, including an elevation correction for the thermodynamic near-surface state (Muñoz-Sabater *et al* 2021).

In addition, we use monthly averaged air temperature and specific humidity at the lowest pressure level from ERA5 reanalysis ($0.25^\circ \times 0.25^\circ$, diel average, 2000–2019) (Hersbach *et al* 2019). Depending on the surface pressure, the height of these atmospheric variables is about 40–100 m. This height is assumed to be above the surface roughness layer (Lee *et al* 2011), although in reality this assumption may be violated over some forest or urban areas (Oke *et al* 2017, Li and Wang 2019, Novick and Katul 2020), which may undermine the validity of Monin–Obukhov similarity theory in calculating the turbulent fluxes.

2.4. Population and Köppen–Geiger climate zones

The Gridded Population of the World, Version 4 (GPWv4): Population Count, Revision 11 at the resolution of 30 arc-second for two single years (2000 and 2020) are used. This dataset is produced by the Center for International Earth Science Information Network at Columbia University (CIESIN 2018). We also use the global map of Köppen–Geiger classification at 1 km resolution (Beck *et al* 2018). In this study, the global climates are divided into four main groups (figure S2(c)): A (tropical), B (arid/dry), C (temperate), and D (continental). None of the 228 megacities are located in the E (polar) category.

2.5. Diagnosing the impact of vegetation trend on the trend of SUHII

Changes in the SUHII are due to the combined effects of vegetation dynamics, changes in anthropogenic heat sources and man-made infrastructures, and large-scale climate change. We quantify the impact of uneven urban and rural vegetation trends on the trend of SUHII based on the TRM method. The TRM method was first developed to attribute the effect of land cover changes on LST using paired flux measurements or climate model simulations (Rigden and Li 2017, Liao *et al* 2018b, Wang *et al* 2019, 2020b, Li *et al* 2019a, Moon *et al* 2020, Wang and Li 2021). In this study, we attribute the vegetation-induced LST change (i.e. the urban-rural LST difference that is solely caused by LAI difference between urban and rural areas, denoted as $SUHII^{LAI}$) to five biophysical factors, namely, albedo (α), aerodynamic resistance (r_a), surface resistance (r_s), emissivity (ε), and the ground heat flux (which is computed as the residual of energy balance and denoted as REB) (Lawrence *et al* 2018, Chen *et al* 2020a), as follows:

$$\begin{aligned}
& \text{SUHII}^{\text{LAI}} \\
&= \frac{\partial T_s}{\partial \text{LAI}} \times (\text{LAI}_u - \text{LAI}_r) = \frac{\partial T_s}{\partial \text{LAI}} \times \text{LAI}_{\text{dif}} \\
&= \left[\begin{aligned} & \left(\frac{\partial T_s}{\partial \alpha} \right) \left(\frac{\partial \alpha}{\partial \text{LAI}} \right) + \left(\frac{\partial T_s}{\partial r_a} \right) \left(\frac{\partial r_a}{\partial \text{LAI}} \right) \\ & + \left(\frac{\partial T_s}{\partial r_s} \right) \left(\frac{\partial r_s}{\partial \text{LAI}} \right) + \left(\frac{\partial T_s}{\partial \varepsilon} \right) \left(\frac{\partial \varepsilon}{\partial \text{LAI}} \right) \\ & + \left(\frac{\partial T_s}{\partial \text{REB}} \right) \left(\frac{\partial \text{REB}}{\partial \text{LAI}} \right) \end{aligned} \right] \\
& \times \text{LAI}_{\text{dif}} \tag{1}
\end{aligned}$$

where $\frac{\partial T_s}{\partial \text{LAI}}$ is the sensitivity of LST to LAI over the reference (i.e. rural areas) (supplementary information), LAI_u and LAI_r are the LAIs in urban and rural areas, respectively, LAI_{dif} is the urban-rural LAI difference. It is stressed that $\text{SUHII}^{\text{LAI}}$ is different from the satellite-observed SUHII that is affected by a variety of other influences as discussed earlier. Since the goal is to quantify the impact of vegetation trends on the trend of SUHII, we replace the LAI_{dif} by the trend in LAI_{dif} (i.e. $\Delta \text{LAI}_{\text{dif}}$):

$$\begin{aligned}
& \Delta \text{SUHII}^{\text{LAI}} \\
&= \left[\begin{aligned} & \left(\frac{\partial T_s}{\partial \alpha} \right) \left(\frac{\partial \alpha}{\partial \text{LAI}} \right) + \left(\frac{\partial T_s}{\partial r_a} \right) \left(\frac{\partial r_a}{\partial \text{LAI}} \right) \\ & + \left(\frac{\partial T_s}{\partial r_s} \right) \left(\frac{\partial r_s}{\partial \text{LAI}} \right) + \left(\frac{\partial T_s}{\partial \varepsilon} \right) \left(\frac{\partial \varepsilon}{\partial \text{LAI}} \right) \\ & + \left(\frac{\partial T_s}{\partial \text{REB}} \right) \left(\frac{\partial \text{REB}}{\partial \text{LAI}} \right) \end{aligned} \right] \\
& \times \Delta \text{LAI}_{\text{dif}} = \frac{\partial \text{SUHII}}{\partial \text{LAI}_{\text{dif}}} \times \Delta \text{LAI}_{\text{dif}} \tag{2}
\end{aligned}$$

where $\Delta \text{SUHII}^{\text{LAI}}$ is the trend in the SUHII induced by the trend in LAI_{dif} and the sensitivity is denoted as $\frac{\partial \text{SUHII}}{\partial \text{LAI}_{\text{dif}}}$.

3. Results and discussion

3.1. Background LAI_{dif} and SUHII

Overall LAI is higher in rural areas than in urban areas (i.e. $\text{LAI}_{\text{dif}} < 0$, figure 1(a)). We divide the world into 11 subcontinental regions (figure S2(b)). Megacities in eastern South America (ESA), eastern North America (ENA), and Oceania (OC) have relatively large LAI_{dif} values ($< -1 \text{ m}^2 \text{ m}^{-2}$, table 1), but the largest LAI_{dif} value is detected in the equatorial megacity of Singapore and Johor Bahru ($-3 \text{ m}^2 \text{ m}^{-2}$). The LAI_{dif} values are also large in coastal regions in eastern South America (ESA) and East Asia (EA) (figure 1(a)). In arid and semi-arid regions, the LAI_{dif} values are close to zero or weakly positive (table 1, figure 1(a)).

For comparison with LAI_{dif} , the daily mean SUHII from Terra MODIS is shown (figure 1(b)). The daily mean SUHII from Terra (overpass time: 10:30 a.m./p.m. local time) agrees with that of Aqua (overpass time: 1:30 p.m./a.m.), with Aqua SUHII having

slightly larger magnitude (slope = 1.05, figure 1(d)). Considering the longer time series and less cloud cover in the morning, we use the daily mean SUHII from Terra for the following analysis. The SUHII is the strongest in North America (i.e. WNA and ENA) (table 1) and is also large in many coastal regions of ESA, EA, southeast Asia, and Europe (figure 1(b)). Notably, we find urban cool islands (i.e. $\text{SUHII} < 0 \text{ K}$) in arid places such as Saharan Africa and West Asia (figure 1(b)). Statistically SUHII is negatively correlated with LAI_{dif} (slope = -0.92 , $p < 0.001$, figure 1(c)) and LAI_{dif} explains 33% of the SUHII variance (figure 1(c)).

3.2. Trends in LAI_{dif}

Of the 228 megacities, 189 show a decreasing trend of LAI_{dif} (becomes more negative) during the peak growing season, 90 of which are statistically significant ($p < 0.05$, figure 2(a)). In contrast, only 39 megacities show an increasing trend in LAI_{dif} , of which only two are statistically significant ($p < 0.05$, figure 2(a)). The absolute and relative values of $\Delta \text{LAI}_{\text{dif}}$ have similar spatial patterns (figures 2(a) and S4), which are nonetheless different from the spatial pattern of the background LAI_{dif} (figure 1(a)). The strongest declines in LAI_{dif} , which exceed $-0.25 \text{ m}^2 \text{ m}^{-2} \text{ decade}^{-1}$ (or $25\% \text{ decade}^{-1}$), occur in East Asia (EA, table 1) where strong greening trends are observed in rural China likely due to land-use management, along with declines in urban greenness due to rapid urbanization (Wang *et al* 2012, Chen *et al* 2019). LAI_{dif} is also declining rapidly in growing megacities such as the Gulf of Guinea in Africa, Southeast Asia, Sydney in Oceania, and Calgary and Edmonton in North America (figure 2(a)).

A decreasing trend of LAI_{dif} may imply one of the following three scenarios: (a) rural greening is faster than urban greening, (b) rural browning is slower than urban browning, or (c) rural areas are greening while urban areas are browning. Our results indicate that 133 of the 228 megacities are greening simultaneously in both urban and rural areas but the rural areas are greening faster (uG-rG), suggesting a slowdown in terms of urbanization. Such megacities are concentrated in ENA, Europe, and extend into coastal regions in EA (figure 2(b)). In addition, 52 megacities show urban browning and rural greening (i.e. uB-rG), reflecting a moderate rate of urbanization. These are distributed worldwide but are almost absent in Europe. Together these two categories (i.e. with negative LAI_{dif} trends) include 185 megacities. Of the remaining 43 megacities, 37 show both urban and rural browning (uB-rB), which imply rapid urbanization, and six show urban greening and rural browning (uG-rB).

3.3. Trends in SUHII

We quantify the SUHII trend caused by the LAI_{dif} trend (i.e. $\Delta \text{SUHII}^{\text{LAI}}$) using the TRM

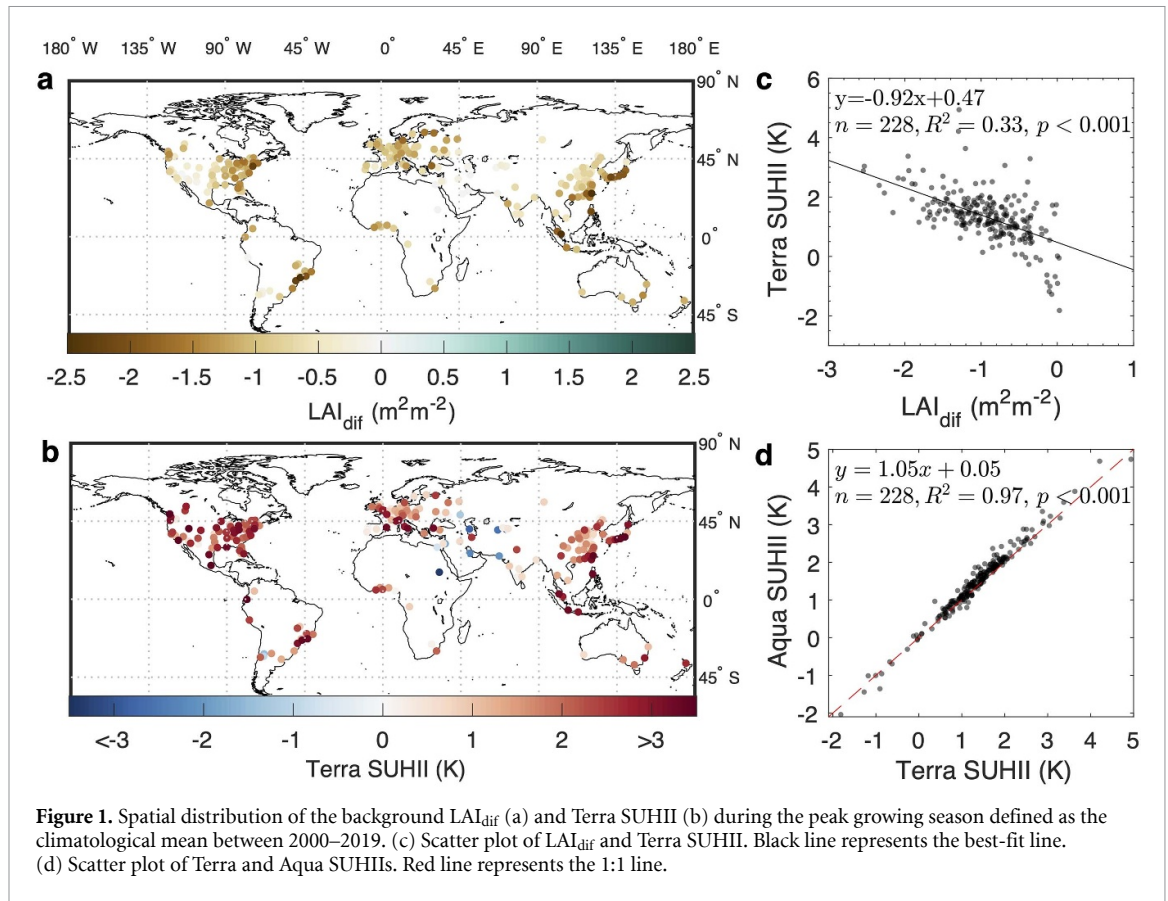


Figure 1. Spatial distribution of the background LAI_{dif} (a) and Terra SUHII (b) during the peak growing season defined as the climatological mean between 2000–2019. (c) Scatter plot of LAI_{dif} and Terra SUHII. Black line represents the best-fit line. (d) Scatter plot of Terra and Aqua SUHIIs. Red line represents the 1:1 line.

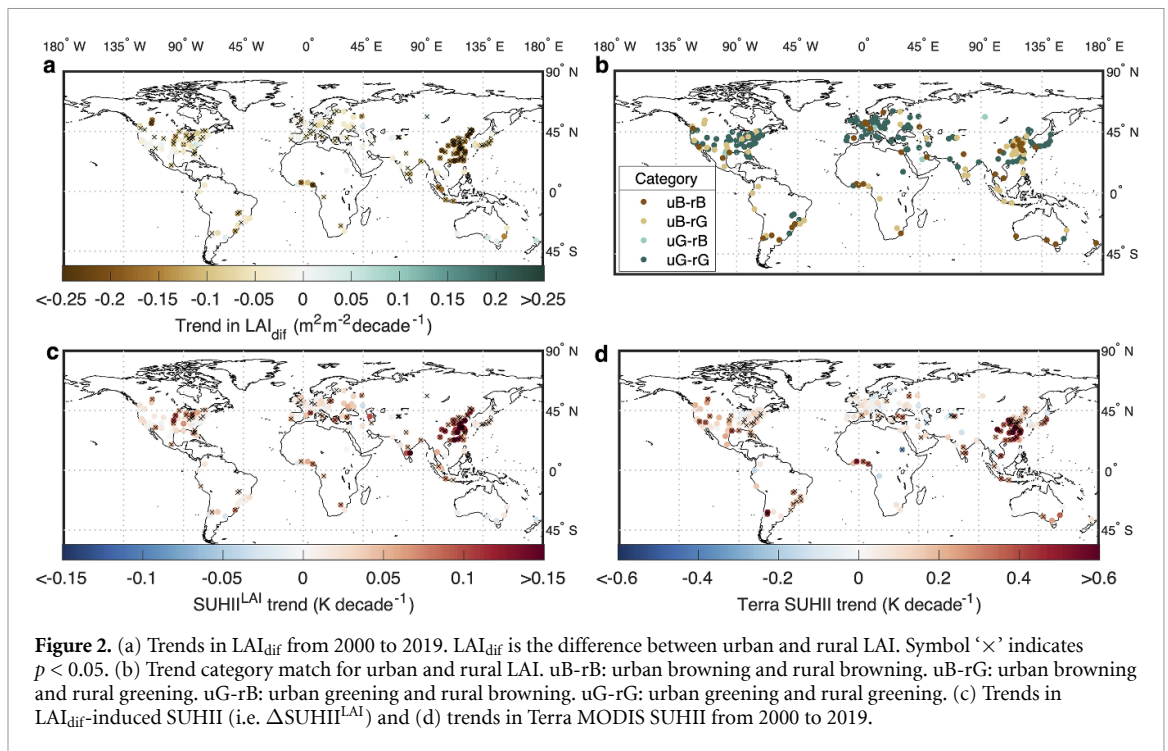
Table 1. Ranking of 11 subcontinental regions by mean background LAI_{dif} and Terra SUHII, trends in LAI_{dif} and LAI-induced SUHII, and population change in the past two decades. The rankings are color-coded in the column direction. Numbers represent mean \pm one standard deviation.

	LAI_{dif} ($m^2 m^{-2}$)	Terra SUHII (K)	ΔLAI_{dif} ($m^2 m^{-2} decade^{-1}$)	$\Delta SUHII^{LAI}$ ($K decade^{-1}$)	$\Delta Population$ (million)	
WNA	-0.68 ± 0.38	1.77 ± 0.88	-0.044 ± 0.051	0.025 ± 0.028	1.00 ± 1.07	1
ENA	-1.23 ± 0.36	1.71 ± 0.38	-0.046 ± 0.038	0.028 ± 0.027	0.47 ± 0.59	2
WSA	-0.66 ± 0.56	1.50 ± 1.80	-0.025 ± 0.032	0.013 ± 0.021	1.84 ± 1.60	3
ESA	-1.36 ± 0.69	1.67 ± 0.62	-0.050 ± 0.049	0.015 ± 0.026	1.38 ± 1.22	4
WEU	-0.99 ± 0.28	1.24 ± 0.56	-0.021 ± 0.032	0.014 ± 0.024	0.39 ± 0.61	5
EEU	-0.90 ± 0.40	0.88 ± 0.66	-0.048 ± 0.034	0.036 ± 0.029	0.23 ± 0.96	6
SSA	-1.02 ± 0.32	1.16 ± 0.55	-0.084 ± 0.076	0.037 ± 0.030	3.22 ± 2.38	7
WCA + SAH	-0.26 ± 0.45	0.15 ± 1.18	-0.014 ± 0.023	0.016 ± 0.031	1.30 ± 1.72	8
SSEA	-1.10 ± 0.83	1.34 ± 0.96	-0.079 ± 0.053	0.060 ± 0.069	6.18 ± 4.04	9
EA	-0.99 ± 0.55	1.38 ± 0.63	-0.116 ± 0.078	0.069 ± 0.059	2.38 ± 4.66	10
OC	-1.12 ± 0.21	1.42 ± 0.40	-0.010 ± 0.078	-0.008 ± 0.019	0.04 ± 0.10	11

WNA: western North America; ENA: Eastern North America; WSA: western South America; ESA: Eastern South America; WEU: western Europe; EEU: eastern Europe; SSA: Sub-Saharan African; WCA + SAH: Western and Central Asia + Saharan Africa; SSEA: South and Southeast Asia; EA: East Asia; OC: Oceania.

method (figure 2(c)). Due to the strongest LAI_{dif} trend, EA shows the largest $\Delta SUHII^{LAI}$ (mean = $0.069 K decade^{-1}$), followed by SSEA (South and Southeast Asia, mean = $0.06 K decade^{-1}$), and SSA (sub-Saharan Africa, mean = $0.037 K decade^{-1}$)

(table 1). These regions have experienced rapid urbanization and population growth over the past 20 years (table 1). Of the top 20 megacities with the largest positive $\Delta SUHII^{LAI}$ globally (mean = $0.14 K decade^{-1}$), 15 are in China. For



individual megacities, Hefei (China) and Chennai (India) rank 1st and 2nd in terms of $\Delta SUHII^{LAI}$ (0.29 and 0.28 $K decade^{-1}$, respectively) (table S1) and both of them show a trend ($\Delta SUHII^{LAI}$) exceeding 20% $decade^{-1}$ (table S1). This is due to rural (cropland) greening and urban browning (i.e. uB-rG) in both megacities, which is reflected in their higher ΔLAI_{dif} (Hefei in EA: $-0.31 m^2 m^{-2} decade^{-1}$, Chennai in SSEA: $-0.11 m^2 m^{-2} decade^{-1}$) compared to the average ΔLAI_{dif} in their respective subcontinent regions (table 1). The opposite vegetation trends in urban and rural areas imply an increase in the urban temperature and a decrease in the rural temperature, which lead to an elevated SUHII.

The spatial patterns of $\Delta SUHII^{LAI}$ and the trend of SUHII (i.e. $\Delta SUHII$) directly computed from Terra MODIS are in reasonable agreement, but the magnitude of $\Delta SUHII^{LAI}$ is on average about one-fourth of $\Delta SUHII$ (figures 2(c) and (d)). The difference between $\Delta SUHII^{LAI}$ and $\Delta SUHII$ highlights that uneven vegetation trends in urban and rural areas are not the sole contributor to the trend in SUHII (Oleson 2012, Li *et al* 2016). Evaluating the role of non-vegetation factors is out of the scope of this study, which requires, at the very least, data of anthropogenic heat fluxes and modeling the urban surface energy budget (Wang and Li 2021). But those are challenging and subject to large uncertainties (Allen *et al* 2011, Oleson 2012, Zhao *et al* 2014, Li *et al* 2016, Jin *et al* 2019, Zheng *et al* 2021). The contribution of anthropogenic heat flux to the SUHII could be 0.75–7.5 K according to a previous fine-resolution modeling study (Wang and Li 2021), which may explain the opposite signs between $\Delta SUHII^{LAI}$ and $\Delta SUHII$ over the U.S. Great Lakes region (figures 2(c)

and (d)). According to the U.S. Energy Information Administration, there is a strong declining trend in energy-related carbon dioxide emissions in the Great Lakes region from 2000 to 2018 (EIA 2021). As a result, the anthropogenic heat flux might be also declining and thus $\Delta SUHII$ is weaker compared to $\Delta SUHII^{LAI}$.

3.4. The sensitivity of SUHII to LAI_{dif}

The sensitivity of SUHII to LAI_{dif} is a marginal sensitivity under the current climatological states. It represents how much the SUHII is altered with a small change in LAI_{dif} . This sensitivity has been shown to reasonably capture temperature changes caused by small perturbations, such as those caused by the two-decade vegetation trends shown above (Chen *et al* 2020a). It should be used with caution for understanding the SUHII which encodes large perturbations (Chen *et al* 2020b). The TRM method decomposes the sensitivity of SUHII to LAI_{dif} (i.e. $\frac{\partial SUHII}{\partial LAI_{dif}}$) into five contributors (figure S5). Surface resistance, which represents the ability to bring water to the surface, dominates $\frac{\partial SUHII}{\partial LAI_{dif}}$ in 177 of the 228 megacities among different biophysical factors (figure 3(b)). Thus, the spatial variability of LAI-induced SUHII changes at the global scale is primarily controlled by changes in the ability of land areas to evaporate water. This finding is consistent with the conclusion of previous studies (Bateni and Entekhabi 2012, Li *et al* 2019a), namely, vegetation changes mainly affect LST through the ET process. The $\frac{\partial SUHII}{\partial LAI_{dif}}$ in the remaining 51 megacities are dominated by aerodynamic resistance. The megacities where $\frac{\partial SUHII}{\partial LAI_{dif}}$ is dominated by aerodynamic resistance have significantly lower aridity index (Pr/PET) than those

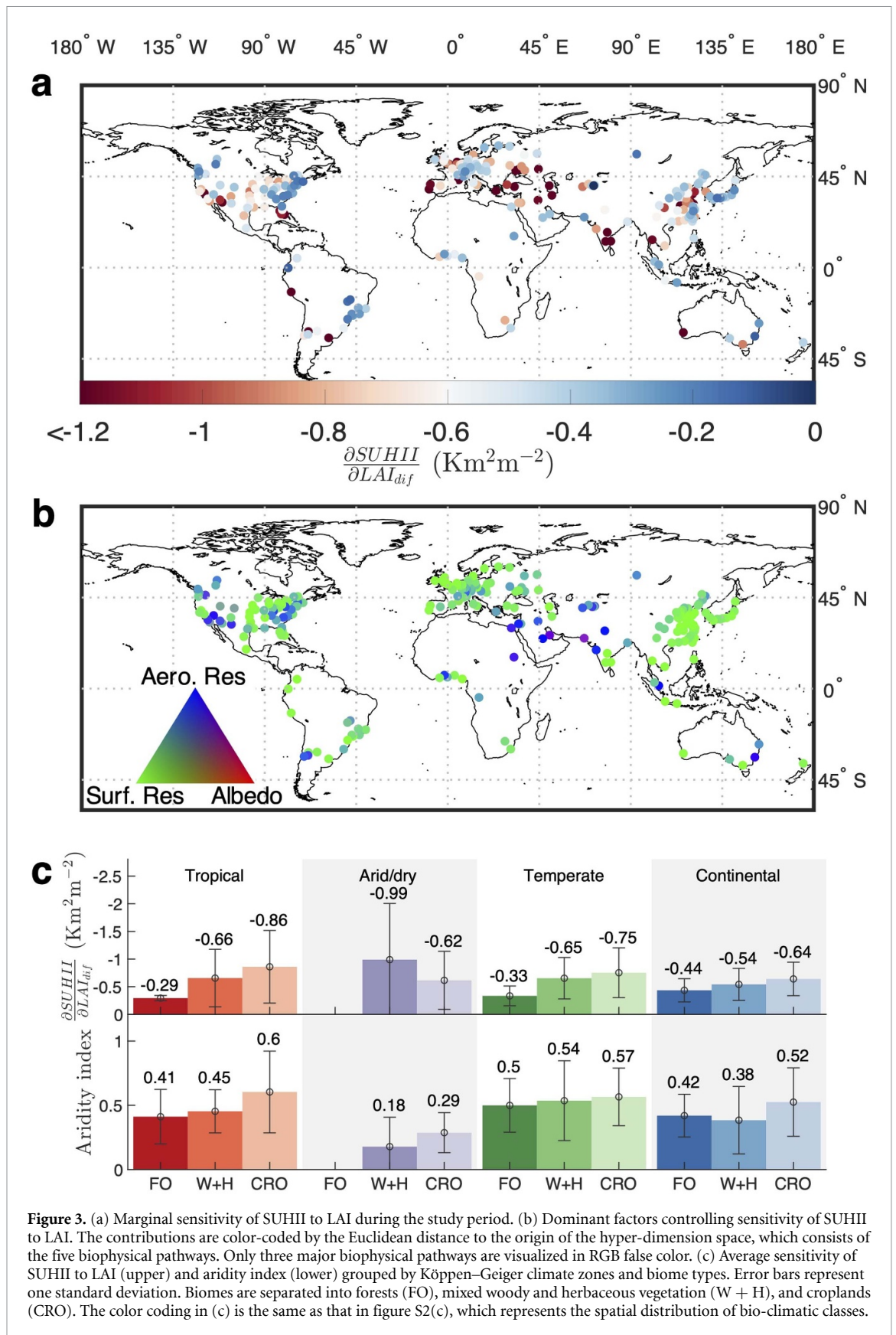


Figure 3. (a) Marginal sensitivity of SUHII to LAI during the study period. (b) Dominant factors controlling sensitivity of SUHII to LAI. The contributions are color-coded by the Euclidean distance to the origin of the hyper-dimension space, which consists of the five biophysical pathways. Only three major biophysical pathways are visualized in RGB false color. (c) Average sensitivity of SUHII to LAI (upper) and aridity index (lower) grouped by Köppen–Geiger climate zones and biome types. Error bars represent one standard deviation. Biomes are separated into forests (FO), mixed woody and herbaceous vegetation (W + H), and croplands (CRO). The color coding in (c) is the same as that in figure S2(c), which represents the spatial distribution of bio-climatic classes.

dominated by surface resistance (mean \pm 1 standard deviation: 0.31 ± 0.27 vs. 0.51 ± 0.27 , two sample t -test: $p < 10^{-5}$). Aerodynamic resistance represents the convective heat transfer efficiency affecting both

sensible heat and latent heat fluxes. Many megacities where $\frac{\partial \text{SUHII}}{\partial \text{LAI}_{\text{dif}}}$ is dominated by aerodynamic resistance are located in arid to semi-arid western United States (Zhao *et al* 2014), Saharan Africa, and West

Asia (figures 3(b) and S2(c)) (Li *et al* 2021). In these megacities, changes in aerodynamic resistance caused by the vegetation trend are more likely to affect SUHII through sensible heat flux. However, for those megacities in the eastern United States where the climate is relatively humid (figures 3(b) and S2(c)), changes in aerodynamic resistance are more likely to affect SUHII through changing the latent heat flux (Chen *et al* 2020a). The contribution of LAI-induced albedo changes is on average about 6% to the $\frac{\partial \text{SUHII}}{\partial \text{LAI}_{\text{dif}}}$ (figure S5), which depends on the sensitivity of light-extinction to LAI change within the vegetation canopy. As expected, contributions from other factors (i.e. ground heat flux and emissivity) are not significant (Chen *et al* 2020a).

We further group the $\frac{\partial \text{SUHII}}{\partial \text{LAI}_{\text{dif}}}$ according to the Köppen–Geiger climate zones and biome types (figure S2(c)). First, SUHII is most sensitive to LAI_{diff} in megacities located in arid/dry areas surrounded by mixed woody and herbaceous biomes (W + H, figure 3(c)). In most of these areas, $\frac{\partial \text{SUHII}}{\partial \text{LAI}_{\text{dif}}}$ is dominated by aerodynamic resistance (figure 3(b)). Second, $\frac{\partial \text{SUHII}}{\partial \text{LAI}_{\text{dif}}}$ increases from megacities surrounded by forests to megacities surrounded by croplands in a given climate regime (except for the arid/dry climate) (figure 3(c)). The higher sensitivity for megacities surrounded by croplands implies that for an equal change in LAI_{diff}, intensification of rural croplands can increase SUHII more strongly. Incidentally, the LAI_{diff} trends are large for cropland-surrounded megacities, especially in the continental and tropical climates (figure S6). As a result of the combined effects of higher sensitivities and larger LAI_{diff} trends, 13 of the top 20 megacities with the largest positive $\Delta \text{SUHII}^{\text{LAI}}$ are surrounded by croplands (table S1).

Why is $\frac{\partial \text{SUHII}}{\partial \text{LAI}_{\text{dif}}}$ higher in megacities surrounded by croplands than those surrounded by forests (figure 3(c))? Due to the relatively low LAI in croplands on average (figure S6), the absorption of photosynthetically active radiation (PAR) is unsaturated. Therefore, compared to natural vegetation, an increase in crop LAI can absorb more PAR, which provides more available energy to trigger the opening of stomata and increases the evaporative cooling, leading to a larger $\frac{\partial \text{SUHII}}{\partial \text{LAI}_{\text{dif}}}$ (Li *et al* 2021). Furthermore, croplands potentially have more water available for ET due to irrigation (D’Odorico *et al* 2020). These combined effects of canopy structure, radiation field, and water availability shape the higher aridity index (i.e. wetter) in croplands than other biomes across different climate zones (figure 3(c)). All of these are consistent with the finding that $\frac{\partial \text{SUHII}}{\partial \text{LAI}_{\text{dif}}}$ is mainly controlled by surface resistance (figure 3(b)). For megacities surrounded by forests, the low $\frac{\partial \text{SUHII}}{\partial \text{LAI}_{\text{dif}}}$ is due to their high background LAI in both rural and urban areas (figure S3). The high background LAI makes the biophysical factors insensitive to LAI due to saturation effects, especially for radiation and surface resistance.

4. Conclusion

In this study, we quantify the biophysical effects of vegetation dynamics on the contrast of LST between urban and rural areas over 228 megacities. Our results show that increases in LAI_{diff} contribute to a quarter of the increasing trends in SUHII. The biophysical effects of vegetation trends on SUHII trends are determined by two major aspects. First, they depend on the magnitude of LAI_{diff} trends, which is a joint effect of human land-use management and climate change such as warming and elevated atmospheric CO₂ (Zhu *et al* 2016, Chen *et al* 2019, Piao *et al* 2020). Trends in LAI_{diff} are most evident in megacities in Asia. Second, vegetation biophysical effects also depend on the sensitivity of SUHII to LAI_{diff}, which is controlled by background climate and biome type. We find that this sensitivity is the strongest in hot-humid megacities surrounded by croplands and in hot-dry megacities surrounded by mixed woody and herbaceous vegetation. However, their dominant mechanisms are different. The former is mainly controlled by surface resistance which affects the latent heat flux, while the latter is mainly controlled by aerodynamic resistance which affects both sensible heat flux and latent heat flux depending on water availability. The high sensitivities suggest that continued cropland intensification and semi-arid woody vegetation encroachment in rural areas may enhance SUHII; while increasing urban vegetation in these megacities can reduce LAI_{diff} and thus mitigate SUHII. The highest background LAI_{diff} and SUHII are concentrated in megacities surrounded by forests in North and South America, but the sensitivity of SUHII to LAI_{diff} is relatively low in these regions because of the high background LAI in urban and rural areas. Therefore, to reduce SUHII by the same amount as in megacities surrounded by croplands, megacities surrounded by forests would need to increase more urban greenness or invoke additional measures such as adopting white roofs and reducing anthropogenic heat emissions.

Data availability statement

The data that support the findings of this study are openly available. MODIS LAI MOD15A2H: <https://doi.org/10.5067/MODIS/MOD15A2H.006>. MODIS LAIMYD15A2H: <https://doi.org/10.5067/MODIS/MYD15A2H.006>. MODIS LST MOD11C3: <https://doi.org/10.5067/MODIS/MOD11C3.006>. MODIS LST MYD11C3: <https://doi.org/10.5067/MODIS/MYD11C3.006>. MODIS Land Cover: <https://doi.org/10.5067/MODIS/MCD12C1.006>. CIESIN Gridded Population of the World: <https://doi.org/10.7927/H4JW8BX5>. Köppen–Geiger climate classification: <https://doi.org/10.1038/sdata.2018.214>. ERA5-Land monthly averaged data: <https://doi.org/10.24381/cds.68d2bb30>. ERA5 monthly

averaged data on pressure levels: <https://doi.org/10.24381/cds.6860a573>. Scripts for the TRM framework are available at <https://doi.org/10.5281/zenodo.5594686>. CESM2/CLM5 release code is available at http://www.cesm.ucar.edu/models/cesm2/release_download.html. R-package for Mann-Kendall test is available at <https://cran.r-project.org/web/packages/zyp/index.html>.

Acknowledgments

C C and T F K are supported by the U.S. Department of Energy, Office of Science, Office of Biological and Environmental Research, Reducing Uncertainties in Biogeochemical Interactions through Synthesis and Computation Scientific Focus Area. T F K acknowledges additional support from the U.S. Department of Energy Early Career Research Program Award #DE-SC0021023. D L is supported by the U.S. Department of Energy, Office of Science, as part of research in Multi-Sector Dynamics, Earth and Environmental System Modelling Program. We thank the National Center for Atmospheric Research (supported primarily by the U.S. National Science Foundation) for providing supercomputing resources. The authors declare no competing interests.


Author contributions

C C designed the study, analyzed the data, and drafted the manuscript. All authors interpreted the results and revised the manuscript.

ORCID iDs

Chi Chen  <https://orcid.org/0000-0002-8079-4079>

Dan Li  <https://orcid.org/0000-0001-5978-5381>

Trevor F Keenan  <https://orcid.org/0000-0002-3347-0258>

References

- Allen L, Lindberg F and Grimmond C S B 2011 Global to city scale urban anthropogenic heat flux: model and variability *Int. J. Climatol.* **31** 1990–2005
- Bateni S M and Entekhabi D 2012 Relative efficiency of land surface energy balance components *Water Resour. Res.* **48** 97–98
- Beck H E, Zimmermann N E, McVicar T R, Vergopolan N, Berg A and Wood E F 2018 Present and future Köppen-Geiger climate classification maps at 1-km resolution *Sci. Data* **5** 180214
- Chakraborty T and Lee X 2019 A simplified urban-extent algorithm to characterize surface urban heat islands on a global scale and examine vegetation control on their spatiotemporal variability *Int. J. Appl. Earth Obs. Geoinf.* **74** 269–80
- Chen C *et al* 2019 China and India lead in greening of the world through land-use management *Nat. Sustain.* **2** 122–9
- Chen C, Li D, Li Y, Piao S, Wang X, Huang M, Gentile P, Nemani R R and Myneni R B 2020a Biophysical impacts of Earth greening largely controlled by aerodynamic resistance *Sci. Adv.* **6** eabb1981
- Chen C, Wang L, Myneni R B and Li D 2020b Attribution of land-use/land-cover change induced surface temperature anomaly: how accurate is the first-order Taylor series expansion? *J. Geophys. Res. Biogeosci.* **125** e2020JG005787
- CIESIN—Center for International Earth Science Information Network at Columbia University 2018 *Gridded population of the world, version 4 (GPWv4): population count, revision 11* (<https://doi.org/10.7927/H4JW8BX5> (Accessed 5 October 2020))
- D’Odorico P, Chiarelli D D, Rosa L, Bini A, Zilberman D and Rulli M C 2020 The global value of water in agriculture *Proc. Natl Acad. Sci.* **117** 21985–93
- EIA 2021 Energy-related CO₂ emission data tables State energy-related carbon dioxide emissions by year, adjusted (2000–2018) (available at: www.eia.gov/environment/emissions/state/ (Accessed 5 October 2020))
- Friedl M A *et al* 2002 Global land cover mapping from MODIS: algorithms and early results *Remote Sens. Environ.* **83** 287–302
- Friedl M A and Sulla-Menashe D 2015 MCD12C1 MODIS/Terra+Aqua land cover type yearly L3 global 0.05Deg CMG V006 (<https://doi.org/10.5067/MODIS/MCD12C1.006> (Accessed 5 October 2020))
- Hansen J, Ruedy R, Sato M and Lo K 2010 Global surface temperature change *Rev. Geophys.* **48** 644–29
- Hersbach H *et al* 2019 ERA5 monthly averaged data on pressure levels from 1979 to present (<https://doi.org/10.24381/cds.6860a573> (Accessed 1 May 2021))
- Imhoff M L, Zhang P, Wolfe R E and Bounoua L 2010 Remote sensing of the urban heat island effect across biomes in the continental USA *Remote Sens. Environ.* **114** 504–13
- Jin K, Wang F, Chen D, Liu H, Ding W and Shi S 2019 A new global gridded anthropogenic heat flux dataset with high spatial resolution and long-term time series *Sci. Data* **6** 139
- Kalnay E and Cai M 2003 Impact of urbanization and land-use change on climate *Nature* **423** 528–31
- Kovats R S and Hajat S 2008 Heat stress and public health: a critical review *Annu. Rev. Public Health* **29** 41–55
- Lawrence D *et al* 2018 Technical description of version 5.0 of the community land model (CLM) pp 1–350 (available at: https://www.cesm.ucar.edu/models/cesm2/land/CLM50_Tech_Note.pdf)
- Lee X *et al* 2011 Observed increase in local cooling effect of deforestation at higher latitudes *Nature* **479** 384–7
- Li D and Bou-Zeid E 2013 Synergistic interactions between urban heat islands and heat waves: the impact in cities is larger than the sum of its parts *J. Appl. Meteorol. Climatol.* **52** 2051–64
- Li D, Bou-Zeid E and Oppenheimer M 2014 The effectiveness of cool and green roofs as urban heat island mitigation strategies *Environ. Res. Lett.* **9** 055002
- Li D, Liao W, Rigden A J, Liu X, Wang D, Malyshev S and Shevliakova E 2019a Urban heat island: aerodynamics or imperviousness? *Sci. Adv.* **5** eaau4299
- Li D, Malyshev S and Shevliakova E 2016 Exploring historical and future urban climate in the Earth system modeling framework: 1. Model development and evaluation *J. Adv. Model. Earth Syst.* **8** 917–35
- Li D and Wang L 2019 Sensitivity of surface temperature to land use and land cover change-induced biophysical changes: the scale issue *Geophys. Res. Lett.* **46** 9678–89
- Li J, Tam C-Y, Tai A P and Lau N-C 2021 Vegetation-heatwave correlations and contrasting energy exchange responses of different vegetation types to summer heatwaves in the Northern Hemisphere during the 1982–2011 period *Agric. For. Meteorol.* **296** 108208
- Li X, Zhou Y, Yu S, Jia G, Li H and Li W 2019b Urban heat island impacts on building energy consumption: a review of approaches and findings *Energy* **174** 407–19
- Liao W *et al* 2018a Stronger contributions of urbanization to heat wave trends in wet climates *Geophys. Res. Lett.* **45** 11 310–7
- Liao W, Li D, Malyshev S, Shevliakova E, Zhang H and Liu X 2021 Amplified increases of compound hot extremes over urban land in China *Geophys. Res. Lett.* **48** e2020GL091252

- Liao W, Rigden A J and Li D 2018b Attribution of local temperature response to deforestation *J. Geophys. Res. Biogeosci.* **123** 1572–87
- Manoli G, Fatichi S, Schlöpfer M, Yu K, Crowther T W, Meili N, Burlando P, Katul G G and Bou-Zeid E 2019 Magnitude of urban heat islands largely explained by climate and population *Nature* **573** 55–60
- Moon M, Li D, Liao W, Rigden A J and Friedl M A 2020 Modification of surface energy balance during springtime: the relative importance of biophysical and meteorological changes *Agric. For. Meteorol.* **284** 107905
- Mora C et al 2017 Global risk of deadly heat *Nat. Clim. Change* **7** 501–6
- Muñoz-Sabater J 2019 ERA5-Land monthly averaged data from 1981 to present (<https://doi.org/10.24381/cds.68d2bb30> (Accessed 5 October 2021))
- Muñoz-Sabater J et al 2021 ERA5-Land: a state-of-the-art global reanalysis dataset for land applications *Earth Syst. Sci. Data Discuss.* **2021** 1–50
- Myneni R, Knyazikhin Y and Park T 2015a MOD15A2H MODIS/terra leaf area index/FPAR 8-day L4 global 500m SIN grid V006 (<https://doi.org/10.5067/MODIS/MOD15A2H.006> (Accessed 5 October 2020))
- Myneni R, Knyazikhin Y and Park T 2015b MYD15A2H MODIS/aqua leaf area index/FPAR 8-day L4 global 500m SIN grid V006 (<https://doi.org/10.5067/MODIS/MYD15A2H.006> (Accessed 5 October 2020))
- Novick K A and Katul G G 2020 The duality of reforestation impacts on surface and air temperature *J. Geophys. Res. Biogeosci.* **125** e2019JG005543
- Oke T R, Mills G, Christen A and Voogt J A 2017 *Urban Climates* (Cambridge: Cambridge University Press)
- Oleson K 2012 Contrasts between urban and rural climate in CCSM4 CMIP5 climate change scenarios *J. Clim.* **25** 1390–412
- Peng S, Piao S, Ciais P, Friedlingstein P, Otlé C, Bréon F-M, Nan H, Zhou L and Myneni R B 2012 Surface urban heat island across 419 global big cities *Environ. Sci. Technol.* **46** 696–703
- Piao S et al 2020 Characteristics, drivers and feedbacks of global greening *Nat. Rev. Earth Environ.* **1** 14–27
- Rigden A J and Li D 2017 Attribution of surface temperature anomalies induced by land use and land cover changes *Geophys. Res. Lett.* **44** 6814–22
- Samanta A, Costa M H, Nunes E L, Vieira S A, Xu L and Myneni R B 2011 Comment on “Drought-induced reduction in global terrestrial net primary production from 2000 through 2009” *Science* **333** 1093
- Schneider A 2012 Monitoring land cover change in urban and peri-urban areas using dense time stacks of Landsat satellite data and a data mining approach *Remote Sens. Environ.* **124** 689–704
- Schneider A et al 2015 A new urban landscape in East–Southeast Asia, 2000–2010 *Environ. Res. Lett.* **10** 034002–16
- Schneider A, Friedl M A and Potere D 2009 A new map of global urban extent from MODIS satellite data *Environ. Res. Lett.* **4** 044003
- Sellers P J et al 1997 Modeling the exchanges of energy, water, and carbon between continents and the atmosphere *Science* **275** 502–9
- Seto K C, Güneralp B and Hutyrá L R 2012 Global forecasts of urban expansion to 2030 and direct impacts on biodiversity and carbon pools *Proc. Natl Acad. Sci. USA* **109** 16083–8
- United Nations Department of Economic and Social Affairs 2019 *World Urbanization Prospects: The 2018 Revision* (New York: United Nations)
- Venter Z S, Chakraborty T and Lee X 2021 Crowdsourced air temperatures contrast satellite measures of the urban heat island and its mechanisms *Sci. Adv.* **7** eabb9569
- Wan Z, Hook S and Hulley G 2015a MOD11C3 MODIS/terra land surface temperature/emissivity monthly L3 global 0.05Deg CMG V006 (<https://doi.org/10.5067/MODIS/MOD11C3.006> (Accessed 5 October 2020))
- Wan Z, Hook S and Hulley G 2015b MYD11C3 MODIS/aqua land surface temperature/emissivity monthly L3 global 0.05Deg CMG V006 (<https://doi.org/10.5067/MODIS/MYD11C3.006> (Accessed 5 October 2020))
- Wang L et al 2012 China’s urban expansion from 1990 to 2010 determined with satellite remote sensing *Chin. Sci. Bull.* **57** 2802–12
- Wang L, Huang M and Li D 2020a Where are white roofs more effective in cooling the surface? *Geophys. Res. Lett.* **47** 202–11
- Wang L and Li D 2021 Urban heat islands during heat waves: a comparative study between Boston and Phoenix *J. Appl. Meteorol. Climatol.* **60** 621–41
- Wang L, Li D, Zhang N, Sun J and Guo W 2020b Surface urban heat and cool islands and their drivers: an observational study in Nanjing, China *J. Appl. Meteorol. Climatol.* **59** 1987–2000
- Wang P, Li D, Liao W, Rigden A and Wang W 2019 Contrasting evaporative responses of ecosystems to heatwaves traced to the opposing roles of vapor pressure deficit and surface resistance *Water Resour. Res.* **55** 4550–63
- Weng Q, Lu D and Schubring J 2004 Estimation of land surface temperature–vegetation abundance relationship for urban heat island studies *Remote Sens. Environ.* **89** 467–83
- Yan K, Park T, Yan G, Chen C, Yang B, Liu Z, Nemani R, Knyazikhin Y and Myneni R 2016a Evaluation of MODIS LAI/FPAR product collection 6. Part 1: consistency and improvements *Remote Sens.* **8** 359–16
- Yan K, Park T, Yan G, Liu Z, Yang B, Chen C, Nemani R, Knyazikhin Y and Myneni R 2016b Evaluation of MODIS LAI/FPAR product collection 6. Part 2: validation and intercomparison *Remote Sens.* **8** 460–26
- Yang Q, Huang X and Tang Q 2019 The footprint of urban heat island effect in 302 Chinese cities: temporal trends and associated factors *Sci. Total Environ.* **655** 652–62
- Yang Q, Huang X, Yang J and Liu Y 2021 The relationship between land surface temperature and artificial impervious surface fraction in 682 global cities: spatiotemporal variations and drivers *Environ. Res. Lett.* **16** 024032
- Yao R, Wang L, Huang X, Gong W and Xia X 2019 Greening in rural areas increases the surface urban heat island intensity *Geophys. Res. Lett.* **46** 2204–12
- Zhao L, Lee X, Smith R B and Oleson K 2014 Strong contributions of local background climate to urban heat islands *Nature* **511** 216–9
- Zheng Z, Zhao L and Oleson K W 2021 Large model structural uncertainty in global projections of urban heat waves *Nat. Commun.* **12** 3736
- Zhou D, Xiao J, Bonafoni S, Berger C, Deilami K, Zhou Y, Frolking S, Yao R, Qiao Z and Sobrino J A 2019 Satellite remote sensing of surface urban heat islands: progress, challenges, and perspectives *Remote Sens.* **11** 48
- Zhou D, Zhang L, Li D, Huang D and Zhu C 2016 Climate–vegetation control on the diurnal and seasonal variations of surface urban heat islands in China *Environ. Res. Lett.* **11** 074009
- Zhu Z et al 2016 Greening of the Earth and its drivers *Nat. Clim. Change* **6** 791–5